Aerodynamic Model-Aided Estimation of Attitude, 3D Wind, Airspeed, AOA, and SSA for High-Altitude Long-Endurance UAV

Wonkeun Youn, Hyoungsik Choi, Am Cho, Sungyug Kim, and Matthew B. Rhudy,

Abstract

This paper proposes a novel dynamic model-aided navigation filter to estimate the safety-critical states of an aircraft including the effect of wind. Aerodynamic coefficients and control signals are used to predict the angular rates. Experimental flight results of a high-altitude long-endurance (HALE) UAV demonstrated improvement in attitude estimation compared to a model-based navigation algorithm that does not consider wind, as well as accurate attitude estimation without using gyroscope signals, demonstrating its effectiveness for analytical redundancy.

Index Terms

Unmanned aerial vehicle (UAV), Aerodynamic model, Attitude estimation, Wind estimation, Angle of attack (AOA), Sideslip angle (SSA), Kalman filter.

I. Introduction

THE appropriate identification of the surrounding air field of aircraft is crucial for the performance and safety of the aircraft [1], [2]. The airspeed, angle of attack (AOA), and sideslip angle (SSA) are the three important parameters that describe the interaction between the aircraft and the surrounding air [3]. Reliable measurements or estimations of AOA and SSA are indispensable for safe flight because pilots are trained to monitor the AOA for stall detection.

Recently, a high-altitude long-endurance (HALE) UAV that can fly optimally at high altitudes (up to 60,000 feet) for a considerable amount of time without landing has gained substantial attention because a HALE UAV is capable of flying on a narrow radius for several months to years based on a solar panel energy supply and storage system at 20 km altitude. Additionally, real-time video can be obtained for surveillance and provides network communication services performed by existing satellites at lower cost [4]. A HALE UAV named the Korea aerospace research institute (KARI)-electrical aerial vehicle (EAV)-3, developed by KARI, was recorded in 2016 as the world's third UAV to successfully fly at stratospheric altitudes at an altitude of 18.5 km [5]. For a video of the flight demonstration of KARI EAV-3, please visit https://www.youtube.com/watch?v=CL-3UtUeRA8.

A HALE UAV is typically designed to have a high aspect ratio [6], fly at a low speed to reach high altitudes, and fly for more than a few days in a single flight because it is difficult to take off and land if the weather or wind conditions are not appropriate. When a HALE UAV is flying at low speed, it tends to drift in response to strong side winds. To prevent this, a HALE UAV should be facing the wind as directly as possible by using appropriate control inputs to steer into the wind. Thus, for a HALE UAV to reach stratospheric altitudes under strong wind influences, it is necessary to continually measure or estimate the wind direction and magnitude to control the aircraft accordingly.

Previous work in the literature has proposed various approaches for the accurate state estimation of UAVs, including airspeed, AOA, and SSA [7]–[9]. Based on the sensor fusion architecture utilized in these filters, these approaches can be divided into two main categories. The first category uses a kinematic model of the system based on multiple sensors, combining the information from accelerometers, gyroscopes, Pitot probes, AOA/SSA vanes, and global navigation satellite system (GNSS). These approaches have successfully demonstrated their effectiveness in several prior studies, such as [10]–[12], and have been a primary means of estimating navigation states within estimation filters.

The second category utilizes dynamic model-aided navigation, including aerodynamic model parameters, in the navigation filter. Dynamic model-aided navigation has been widely investigated to estimate the position, velocity, attitude, and bias states of the UAV [13]–[15]. Table I presents comprehensive lists of example applications based on dynamic filters for the state estimation of various UAV applications such as rotary wing, fixed-wing, and multicopter vehicles. Here, we focused on the fixed-wing navigation filter, herein addressing airspeed and AOA/SSA. In [22], [23], the estimation framework utilizing the

Wonkeun Youn, Hyoungsik Choi, Am cho, and Sungyug Kim are with the UAV System Division, Aeronautics Research and Development Head Office, Korea Aerospace Research Institute, Yuseong-gu, Daejeon, 34133, Republic of Korea (e-mail: wkyoun@kari.re.kr, chs@kari.re.kr, cho1838@kari.re.kr, kkisy@kari.re.kr). Matthew Rhudy is with the Division of Engineering, Business, and Computing at the Pennsylvania State University, Reading, PA 19610, USA (e-mail: mbr5002@psu.edu). (corresponding author to provide phone: +1-610-396-6389; e-mail: mbr5002@psu.edu).

TABLE I
The summary of the model-aided UAV navigation applications

References	UAV	States	Method
[16]	multicopter	position, velocity (body), attitude	Utilizing the thrust model for predicting the z-axis acceleration
[17]	multicopter	velocity (body), attitude, wind (2D)	Utilizing IMU and dynamic model (simulation)
[18], [19]	multicopter	attitude(roll, pitch), velocity (body x, y), biases	Utilizing IMU, monocular camera, and dynamic model
[20]	multicopter	velocity (body), attitude, altitude, biases	Utilizing IMU, aerodynamic model, magnetometer, and optical flow
[21]	rotary wing	position, velocity, attitude, biases	Utilizing LASER range finder and both kinematic and aerodynamic models (simulation)
[13]	fixed-wing	position, velocity, attitude, biases	Utilizing force and moment aerodynamic coefficient
[15]	fixed-wing	position, velocity, attitude, biases	Utilizing force and moment aerodynamic coefficient (simulation)
[22]	fixed-wing	AOA, SSA	Without direct flow angle and GNSS measurement using aerodynamic model
[23]	fixed-wing	AOA, SSA, wind (3D)	Without direct flow angle and GNSS measurement using aerodynamic model
[24]	fixed-wing	position, velocity (body), wind (3D), attitude, biases	Utilizing kinematic and aerodynamic model (simulation)
[25]	fixed-wing	position, velocity (body), attitude, biases	Utilizing kinematic and aerodynamic model (simulation)
[26]	fixed-wing	airspeed, AOA, SSA, wind (2D)	Without ADS utilizing the GNSS, IMU, and aerodynamic model
Proposed	fixed-wing (HALE)	3D wind, attitude, airspeed, AOA, SSA, biases	Utilizing ADS, IMU, GNSS, and aerodynamic model

partial aerodynamic parameter of the UAV for AOA and SSA has been proposed without AOA/SSA vanes. In [26], GNSS, IMU, and a low-fidelity model of the aircraft dynamics are utilized in the cascaded Kalman filters to estimate the airspeed, AOA, and SSA without a Pitot-static air data system.

Considering that aerodynamic parameter identification is the prerequisite for the design/verification of a HALE UAV and since control input is always available and is not susceptible to signal interference due to multipathing or jamming, a dynamic model-aided approach is an attractive analytical redundancy solution in case of faults for kinematic-model-based navigation filters [27]. Thus, we focused on the development of a dynamic filter in this paper. In addition, given that the surrounding wind impact on a HALE UAV is more significant than that for small UAVs, which fly at low altitude [28], accurate 3D wind, AOA, and SSA estimations are critical. However, existing studies based on the dynamic model have rarely considered 3D wind effects [13], [15], [22]–[26].

In summary, minimal research has investigated the feasibility of aerodynamic models for attitude estimation in addition to 3D wind, airspeed, AOA, and SSA. Additionally, note that the accurate estimation of the attitude is also indispensable for the stable flight of UAVs. Therefore, in this paper, we propose a novel aerodynamic model-based navigation filter for the estimation of attitude, 3D wind, airspeed, AOA, and SSA. This study may be the first to attempt to estimate the aforementioned states using a dynamic model of a HALE UAV verified through long-duration flight tests (i.e., up to 8 hours). More importantly, this study successfully demonstrated the feasibility of state estimation using the proposed algorithm for analytical redundancy for gyroscopes when the gyroscope signals are totally unavailable.

Unlike previous studies [13], [15], [22]–[26], the proposed algorithm is newly formulated with the minimum number of states (without position states) that are critical for safe flight to simplify the implementation. In addition, 3D wind effects were considered in this study, which have not often been considered within aerodynamic model based methods. The proposed algorithm builds upon our previous work proposed in [29], in which only the attitude is estimated by the aircraft aerodynamic model in simulation. This work differs from [29] in that the effects of the 3D wind components are included as states in the proposed filter. These states are modelled using a random walk (RW) model, which has been determined to be an effective model for wind states for fixed-wing aircraft, e.g., see [11]. The estimation performance of the proposed model-aided algorithm is compared with a previous algorithm [29] that does not consider wind and is validated by a long flight of a HALE UAV that reached an altitude of approximately 14 km. In addition, the 3D wind effect on the estimation result is thoroughly analyzed through two different flight tests.

The remainder of this paper is organized as follows. The preliminary definitions of the attitude, gyroscope, and accelerometer measurements are presented in Section II. The proposed dynamic-model-aided navigation filter is formulated in Section III. Section IV presents the nonlinear estimation algorithm. Section V briefly describe the experimental setup. Section VI presents the results and discussion. In Section VII, the conclusions are drawn.

II. Preliminary Definitions

The attitude can be expressed by the unit quaternion as follows:

$$\mathbf{q} = q_w + q_x\mathbf{i} + q_y\mathbf{j} + q_z\mathbf{k} = \begin{bmatrix} q_w \\ \mathbf{q}_v \end{bmatrix} = \begin{bmatrix} \cos(\gamma/2) \\ \mathbf{e}_x\sin(\gamma/2) \\ \mathbf{e}_y\sin(\gamma/2) \\ \mathbf{e}_z\sin(\gamma/2) \end{bmatrix} \tag{1}$$

where q_w and $\mathbf{q}_v = q_x\mathbf{i}+q_y\mathbf{j}+q_z\mathbf{k}$ denote the real part and vector part of the quaternion, respectively. γ and $\bar{\mathbf{e}} = [\mathbf{e}_x,\ \mathbf{e}_y,\ \mathbf{e}_z]^T$ refer to the rotation angle and rotation axis, respectively [30].

The quaternion multiplication $\otimes$ is given by

$$\mathbf{p} \otimes \mathbf{q} = \begin{bmatrix} p_w q_w - \mathbf{p}_v{}^T\mathbf{q}_v \\ p_w\mathbf{q}_v + q_w\mathbf{p}_v + \mathbf{p}_v \times \mathbf{q}_v \end{bmatrix}. \tag{2}$$

The superscripts $\{n\}$ and $\{b\}$ denote the navigation frame and body-fixed frame of the strapdown IMU, respectively. The origin of the navigation frame $\{n\}$ is within the HALE UAV, the axis are aligned with north, east, and down (NED) directions, thus also called local NED frame. The body-fixed frame $\{b\}$ is attached to the HALE UAV and its origin is located at the center of gravity. A vector $\mathbf{v}^n$ can be expressed through a rotation of a vector $\mathbf{v}^b$ as follows: [31]:

$$\mathbf{v}^n = \mathbf{R}_b^n(\mathbf{q})\mathbf{v}^b \tag{3}$$

where the rotation matrix $\mathbf{R}_b^n(\mathbf{q}) \in \mathrm{SO}(3)$ refers to the rotation matrix from the body frame to the navigation frame as follows:

$$\mathbf{R}_b^n(\mathbf{q}) = \begin{bmatrix} q_w^2 + q_x^2 - q_y^2 - q_z^2 & 2(q_x \cdot q_y - q_w \cdot q_z) & 2(q_x \cdot q_z - q_w \cdot q_y) \\ 2(q_x \cdot q_y + q_w \cdot q_z) & q_w^2 - q_x^2 + q_y^2 - q_z^2 & 2(q_y \cdot q_z + q_w \cdot q_x) \\ 2(q_x \cdot q_z - q_w \cdot q_y) & 2(q_y \cdot q_z + q_w \cdot q_x) & q_w^2 - q_x^2 - q_y^2 - q_z^2 \end{bmatrix}. \tag{4}$$

The unit quaternion can be expressed by the corresponding Euler angles $[\phi,\ \theta,\ \psi]^T$, where ϕ, θ, and ψ refer to the roll, pitch, and yaw, respectively, as follows:

$$\mathbf{q} = \begin{bmatrix} \cos(\phi/2)\cos(\theta/2)\cos(\psi/2) + \sin(\phi/2)\sin(\theta/2)\sin(\psi/2) \\ \sin(\phi/2)\cos(\theta/2)\cos(\psi/2) - \cos(\phi/2)\sin(\theta/2)\sin(\psi/2) \\ \cos(\phi/2)\sin(\theta/2)\cos(\psi/2) + \sin(\phi/2)\cos(\theta/2)\sin(\psi/2) \\ \cos(\phi/2)\cos(\theta/2)\sin(\psi/2) - \sin(\phi/2)\sin(\theta/2)\cos(\psi/2) \end{bmatrix}. \tag{5}$$

Conversely, the Euler angles can be obtained from the corresponding unit quaternion as follows:

$$\begin{bmatrix} \phi \\ \theta \\ \psi \end{bmatrix} = \begin{bmatrix} \mathrm{atan2}\left(\frac{2(q_w q_x + q_y q_z)}{1-2(q_x^2+q_y^2)}\right) \\ \mathrm{asin}\left(2(q_w q_y - q_z q_x)\right) \\ \mathrm{atan2}\left(\frac{2(q_w q_z + q_x q_y)}{1-2(q_y^2+q_z^2)}\right) \end{bmatrix}. \tag{6}$$

1) Gyroscope: The three-axis gyroscope measures the angular rate about each of the three axes as follows [32]:

$$\boldsymbol{\omega}_m = \boldsymbol{\omega}_t + \boldsymbol{\omega}_{bt} + \boldsymbol{\omega}_n \tag{7}$$

where $\{p_m, q_m, r_m\} = \boldsymbol{\omega}_m \in \mathbb{R}^3$ are the measured angular rate signals, $\boldsymbol{\omega}_t$, $\boldsymbol{\omega}_{bt}$, and $\boldsymbol{\omega}_n \in \mathbb{R}^3$ are the true angular rate signal, slowly varying bias term of the gyroscope, and zero-mean Gaussian noise, respectively.

2) Accelerometer: The three-axis accelerometer measures the acceleration signal as follows [33]:

$$\mathbf{a}_m = \mathbf{R}_b^n(\mathbf{q})^T(\mathbf{a}_t - \mathbf{g}) + \mathbf{a}_{bt} + \mathbf{a}_n \tag{8}$$

where $\{a_{mx}, a_{my}, a_{mz}\} = \mathbf{a}_m \in \mathbb{R}^3$ are the measured acceleration, $\mathbf{g} \in \mathbb{R}^3$ is the gravitational acceleration in the navigation frame, and $\mathbf{a}_t$, $\mathbf{a}_{bt}$, and $\mathbf{a}_n \in \mathbb{R}^3$ are the true acceleration, slowly varying bias term, and zero-mean Gaussian noise, respectively.

In this study, the following discrete-time nonlinear state space system is considered [34]:

$$\mathbf{x}_k = f(\mathbf{x}_{k-1}, \mathbf{u}_k, \mathbf{w}_k) \tag{9}$$

$$\mathbf{z}_k = h(\mathbf{x}_k, \mathbf{v}_k) \tag{10}$$

where $\mathbf{x}_k \in \mathbb{R}^n$, $\mathbf{u}_k \in \mathbb{R}^l$, and $\mathbf{z}_k \in \mathbb{R}^m$ are the state, input, and measurement at time k, respectively, and $f(\cdot)$ and $h(\cdot)$ refer to the state dynamic and observation equations, respectively. The process noise $\mathbf{w}_k$ and measurement noise $\mathbf{v}_k$ are assumed to be uncorrelated, white, zero-mean Gaussian noise as follows:

$$\begin{aligned} \mathbf{w}_k &\sim N(0, \mathbf{Q}_k) \\ \mathbf{v}_k &\sim N(0, \mathbf{R}_k) \\ \mathrm{E}\left[\mathbf{w}_k \mathbf{v}_k^T\right] &= 0 \end{aligned} \tag{11}$$

where $N(\boldsymbol{\mu}_k, \sum_k)$ refers to a Gaussian distribution with a mean of $\boldsymbol{\mu}_k$ and a covariance of $\sum_k$.

III. Dynamic Model-Aided State Estimation

A. Problem Formulation

The state $\mathbf{x}$ and input $\mathbf{u}$ are formulated as follows:

$$\mathbf{x} = [V \;\; \alpha \;\; \beta \;\; p \;\; q \;\; r \;\; \delta\mathbf{p} \;\; \mathbf{a}_b \;\; \boldsymbol{\omega}_b \;\; \mathbf{v}_w^n] \;\in\; \mathbb{R}^{18} \tag{12}$$

$$\mathbf{u} = [a_{mx} \;\; a_{my} \;\; a_{mz} \;\; \boldsymbol{\delta}_E \;\; \boldsymbol{\delta}_A \;\; \boldsymbol{\delta}_R] \;\in\; \mathbb{R}^{6} \tag{13}$$

where V, α, and β denote the airspeed, AOA, and SSA, respectively; $\{p, q, r\} \in \boldsymbol{\omega}$ are the angular rates in the body-fixed frame; $\delta\mathbf{p}$ denotes the generalized Rodrigues parameter (GRP) representing the attitude error; $\{a_{bx}, a_{by}, a_{bz}\} \in \mathbf{a}_b$ and $\{\omega_{bx}, \omega_{by}, \omega_{bz}\} \in \boldsymbol{\omega}_b$ are the accelerometer and gyroscope biases, respectively, in the body-fixed frame; $\{\mathbf{v}_{wn}, \mathbf{v}_{we}, \mathbf{v}_{wd}\} \in \mathbf{v}_w$ are the navigation frames of the north, east, and down vectors of the 3-dimensional wind states; $\{a_{mx}, a_{my}, a_{mz}\} = \mathbf{a}_m$ are the measured accelerations. $\boldsymbol{\delta}_E$, $\boldsymbol{\delta}_A$, and $\boldsymbol{\delta}_R$ are the control input commands for elevator, aileron, and rudder deflection, respectively. Note that the time index k is omitted here for simplicity.

B. State Dynamic Equations

The dynamic equations related to the state airspeed V, AOA α, and SSA β can be formulated with the input of the measured accelerations as follows [35], [36]:

$$\begin{aligned}\dot{V} = {} & (a_{mx} - a_{bx})\cos\alpha\cos\beta + (a_{my} - a_{by})\sin\beta \\ & + (a_{mz} - a_{bz})\sin\alpha\cos\beta + g\Big(-\cos\alpha\cos\beta\sin\theta \\ & + \sin\beta\sin\phi\cos\theta + \sin\alpha\cos\beta\cos\phi\cos\theta\Big)\end{aligned} \tag{14}$$

$$\begin{aligned}\dot{\alpha} = {} & \frac{1}{V\cos\beta}\Big(-(a_{mx} - a_{bx})\sin\alpha + (a_{mz} - a_{bz})\cos\alpha \\ & g\left(\sin\alpha\sin\theta + \cos\alpha\cos\phi\cos\theta\right)\Big) + (q_m - \omega_{by}) \\ & + \Big((p_m - \omega_{bx})\cos\alpha + (r_m - \omega_{bz})\sin\alpha\Big)\tan\beta\end{aligned} \tag{15}$$

$$\begin{aligned}\dot{\beta} = {} & \frac{1}{V}\Big(-(a_{mx} - a_{bx})\cos\alpha\sin\beta + (a_{my} - a_{by})\cos\beta \\ & -(a_{mz} - a_{bz})\sin\alpha\sin\beta + g\left(\cos\alpha\sin\beta\sin\theta\right. \\ & \left.+\cos\beta\cos\theta\sin\phi - \sin\alpha\sin\beta\cos\phi\cos\theta\right)\Big) \\ & + (p_m - \omega_{bx})\sin\alpha - (r_m - \omega_{bz})\cos\alpha.\end{aligned} \tag{16}$$

where g denotes the acceleration due to gravity, which is assumed constant as $9.80665\,\mathrm{m/s^2}$.

The dynamic equation related to the angular rates p, q, and r can be obtained through the moment equation of the UAV as follows [35], [36]:

$$\begin{bmatrix}\dot{p}\\ \dot{q}\\ \dot{r}\end{bmatrix} = \mathbf{M}_1\begin{bmatrix}p^2\\ q^2\\ r^2\end{bmatrix} + \mathbf{M}_2\begin{bmatrix}qr\\ pr\\ pq\end{bmatrix} + \frac{1}{2}\rho V^2\mathbf{M}_0\begin{bmatrix}C_l b\\ C_m\bar{c}\\ C_n b\end{bmatrix} \tag{17}$$

where ρ is the air density, and S, b, and $\bar{c}$ denote the wing area, wing span, and mean aerodynamic chord, respectively. The matrices $\mathbf{M}_0$, $\mathbf{M}_1$, and $\mathbf{M}_2$ are defined by [35], [36]

$$\begin{aligned}\mathbf{M}_0 = {} & \frac{1}{\det(\mathbf{I})} \\ & \cdot\begin{bmatrix}I_{yy}I_{zz} - I_{yz}I_{yz} & I_{xy}I_{zz} + I_{yz}I_{xz} & I_{xy}I_{yz} + I_{yy}I_{xz}\\ I_{xy}I_{zz} + I_{yz}I_{xz} & I_{xx}I_{zz} + I_{xz}I_{xz} & I_{yz}I_{xx} + I_{yz}I_{xz}\\ I_{xy}I_{yz} + I_{yy}I_{xz} & I_{yz}I_{xx} + I_{xy}I_{xz} & I_{xx}I_{yy} + I_{xy}I_{xy}\end{bmatrix}\end{aligned} \tag{18}$$

$$\mathbf{M}_1 = \mathbf{M}_0\begin{bmatrix}0 & -I_{yz} & -I_{yz}\\ -I_{xz} & 0 & -I_{xz}\\ -I_{xy} & -I_{xy} & 0\end{bmatrix} \tag{19}$$

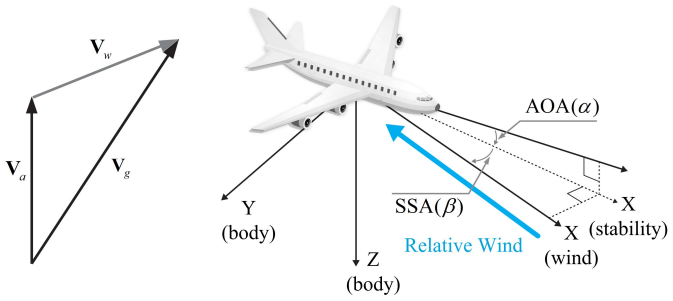

Fig. 1: Relationship between ground speed $\mathbf{v}_g$, airspeed $\mathbf{v}_a$, and wind velocities $\mathbf{v}_w$ in the navigation frame [1].

$$\mathbf{M}_2 = \mathbf{M}_0 \begin{bmatrix} I_{yy} - I_{zz} & -I_{xy} & I_{xz} \\ I_{xy} & I_{zz} - I_{xx} & -I_{yz} \\ -I_{xz} & I_{yz} & I_{xx} - I_{yy} \end{bmatrix} \tag{20}$$

where $\mathbf{I}$ denotes the moment of inertia matrix. I_{ii} and I_{ij} denote the moment of inertia about the i-axis and the product of inertia about the i-axis and j-axis, respectively.

$$\mathbf{I} = \begin{bmatrix} I_{xx} & -I_{xy} & -I_{xz} \\ -I_{xy} & I_{yy} & -I_{yz} \\ -I_{xz} & -I_{yz} & I_{zz} \end{bmatrix} \tag{21}$$

where C_l, C_m, and C_n denote the aerodynamic rolling, pitching, and yawing moments, respectively, as follows [35], [36]:

$$\begin{aligned} C_l &= c_{l0} + c_{l\beta}\beta + c_{lp}\frac{b}{2V}p + c_{lr}\frac{b}{2V}r + c_{l\delta_A}\delta_A + c_{l\delta_R}\delta_R \\ C_m &= c_{m0} + c_{m\alpha}\alpha + c_{mq}\frac{\bar{c}}{2V}p + c_{m\delta_E}\delta_E \\ C_n &= c_{n0} + c_{n\beta}\beta + c_{np}\frac{b}{2V}p + c_{nr}\frac{b}{2V}r + c_{n\delta_A}\delta_A + c_{n\delta_R}\delta_R. \end{aligned} \tag{22}$$

The attitude dynamic equation can be defined as follows [37]:

$$\dot{\mathbf{q}} = \frac{1}{2}\mathbf{q} \otimes \boldsymbol{\omega}. \tag{23}$$

The dynamic equations for the accelerometer and gyroscope biases are modeled utilizing a first-order Gauss-Markov (GM) noise model [11], [12]. In our previous study [38], the Allan variance method was implemented to obtain the statistical parameters of the first-order GM noise model on each axis of the IMU, therein involving two parameters such as a variance of the wide band sensor noise and a time constant. Based on the obtained model, the dynamic equations for the accelerometer and gyroscope biases can be expressed by [12]

$$\begin{aligned} \mathbf{a}_{b,k} &= \mathbf{a}_{b,k-1} \cdot e^{\frac{-T_s}{\tau_a}} + \mathbf{w}^a_{k-1} \\ \boldsymbol{\omega}_{b,k} &= \boldsymbol{\omega}_{b,k-1} \cdot e^{\frac{-T_s}{\tau_\omega}} + \mathbf{w}^\omega_{k-1} \end{aligned} \tag{24}$$

where τ_a and τ_ω denote the correlation time of the GM model for the accelerometer and gyroscope biases. respectively, and $\mathbf{w}^a_{k-1}$ and $\mathbf{w}^\omega_{k-1}$ refer to the zero-mean Gaussian process noise for the accelerometer and gyroscope biases, respectively. T_s refers to the sampling time interval of the IMU.

The dynamic equations for the wind states are assumed to be an RW process, which has been widely adopted in previous works, as follows [12]:

$$\mathbf{v}^n_{w,k} = \mathbf{v}^n_{w,k-1} + \mathbf{w}^w_{k-1} \tag{25}$$

where $\mathbf{w}^w_{k-1}$ refers to the zero-mean Gaussian process noise for the wind velocity. While other more accurate wind models could be considered, e.g. see [11], negligible performance improvement is expected.

C. Measurement Equations

In this paper, the measurements consist of the airspeed V_m, AOA α_m, SSA β_m, angular rates (p_m, q_m, r_m) from the gyroscope, and the velocity measurement $\mathbf{v}^n_g$ from the GNSS receiver. The measurements $\mathbf{z}$ are defined as follows:

$$\mathbf{z} = \begin{bmatrix} V_m & \alpha_m & \beta_m & p_m & q_m & r_m & \mathbf{v}^n_g \end{bmatrix} \tag{26}$$

where $\left\{\mathbf{v}_{g,n}^n, \mathbf{v}_{g,e}^n, \mathbf{v}_{g,d}^n\right\} \in \mathbf{v}_g^n$ are the north, east, and down velocity from the GNSS receiver in the navigation frame. The wind triangular relationships between the ground speed $\mathbf{v}_g$, airspeed $\mathbf{v}_a$, and wind velocity $\mathbf{v}_w$ are illustrated in Fig. 1. Utilizing the wind triangular relationship, the ground speed $\mathbf{v}_g^n$ measured from the GNSS receiver can be formulated with respect to V, α, β, and $\mathbf{v}_w^n$ as follows [39]:

$$\mathbf{v}_g^n = \mathbf{R}_b^n(\mathbf{q})\mathbf{v}_a^b + \mathbf{v}_w^n \tag{27}$$

where

$$\mathbf{v}_a^b = \begin{bmatrix} u \\ v \\ w \end{bmatrix}_b = \begin{bmatrix} V\cos\alpha\cos\beta \\ V\sin\beta \\ V\sin\alpha\cos\beta \end{bmatrix}. \tag{28}$$

IV. Nonlinear State Estimation

The UKF was chosen in this study due to its ease of implementation because it does not require the computation of the Jacobian matrices. In this paper, the standard augmented UKF is adopted [40], [41].

$$\begin{cases} \lambda_u = \alpha_u^2(L+\kappa_u) - L \\ \eta_0^m = \lambda_u/(L+\lambda_u) \\ \eta_0^c = \lambda_u/(L+\lambda_u) + 1 - \alpha_u^2 + \beta_u \\ \eta_i^m = \eta_i^c = 1/[2(L+\lambda_u)], \ i = 1, \cdots, 2L. \end{cases} \tag{29}$$

where α_u, β_u, κ_u, and λ_u refer to the scaling factors, and η_i^m and η_i^c denote the resulting weight vectors for the i-th sigma point of the mean and covariance, respectively [40], [41].

The parameter λ_u, the prior mean $\hat{\mathbf{x}}_{k-1|k-1}$, and the covariance $\mathbf{P}_{k-1|k-1}$ are then used to generate $2L+1$ sigma points as follows:

$$\begin{aligned} \boldsymbol{\chi}_{i,k-1} = \ & \hat{\mathbf{x}}_{k-1|k-1} \\ & + \begin{cases} 0 & \text{for } i = 0 \\ \sqrt{(L+\lambda_u)}\sqrt{\mathbf{P}_{k-1|k-1}^a} & \text{for } i = 1, \cdots, L \\ -\sqrt{(L+\lambda_u)}\sqrt{\mathbf{P}_{k-1|k-1}^a} & \text{for } i = L, \cdots, 2L. \end{cases} \end{aligned} \tag{30}$$

where L is the length of the state vector. The augmented covariance matrix $\mathbf{P}_{k-1|k-1}^a$ is defined by

$$\mathbf{P}_{k-1|k-1}^a = \begin{bmatrix} \mathbf{P}_{k-1} & 0 \\ 0 & \mathbf{Q}_{k-1}. \end{bmatrix} \tag{31}$$

The sigma point $\boldsymbol{\chi}_{i,k-1}$ is fed into the state dynamic equations to obtain the predicted sigma points, and the predicted state $\hat{\mathbf{x}}_{k|k-1}$ and its covariance $\mathbf{P}_{k|k-1}$ can be computed by

$$\hat{\boldsymbol{\chi}}_{i,k|k-1} = f\left(\boldsymbol{\chi}_{i,k-1}, \ \mathbf{u}_k\right), \ \ i = 0, \ 1, \cdots, \ 2L \tag{32}$$

$$\hat{\mathbf{x}}_{k|k-1} = \sum_{i=0}^{2L} \eta_i^m \, \hat{\boldsymbol{\chi}}_{i,k|k-1} \tag{33}$$

$$\mathbf{P}_{k|k-1} = \sum_{i=0}^{2L} \eta_i^c (\hat{\boldsymbol{\chi}}_{i,k|k-1} - \hat{\mathbf{x}}_{k|k-1})(\hat{\boldsymbol{\chi}}_{i,k|k-1} - \hat{\mathbf{x}}_{k|k-1})^T. \tag{34}$$

Then, new sigma points $\boldsymbol{\chi}_{i,k|k-1}$ are generated from $\hat{\mathbf{x}}_{k|k-1}$ and its covariance $\mathbf{P}_{k|k-1}$ in the same way as (30), and the generated sigma points for measurement can be defined as

$$\hat{\boldsymbol{\psi}}_{i,k|k-1} = h(\boldsymbol{\chi}_{i,k|k-1}, \ \mathbf{u}_k), \ i = 0, \ 1, \cdots, \ 2L. \tag{35}$$

Then, the predicted measurement $\hat{\mathbf{z}}_{k|k-1}$, its corresponding covariance matrix $\mathbf{P}_{zz,k}$, and the cross-covariance between the predicted state and measurement $\mathbf{P}_{xz,k}$ can be expressed as

$$\hat{\mathbf{z}}_{k|k-1} = \sum_{i=0}^{2L} \eta_i^m \, \hat{\boldsymbol{\psi}}_{i,k|k-1} \tag{36}$$

$$\mathbf{P}_{zz,k} = \sum_{i=0}^{2L} \eta_i^c (\hat{\boldsymbol{\psi}}_{i,k|k-1} - \hat{\mathbf{z}}_{k|k-1})(\hat{\boldsymbol{\psi}}_{i,k|k-1} - \hat{\mathbf{z}}_{k|k-1})^T + \mathbf{R}_{k-1}. \tag{37}$$

$$\mathbf{P}_{xz,k} = \sum_{i=0}^{2L} \eta_i^c (\hat{\boldsymbol{\chi}}_{i,k|k-1} - \hat{\mathbf{x}}_{k|k-1})(\hat{\boldsymbol{\psi}}_{i,k|k-1} - \hat{\mathbf{z}}_{k|k-1})^T. \tag{38}$$

The state estimate $\hat{\mathbf{x}}_{k|k}$ and corresponding error state covariance matrix $\mathbf{P}_{k|k}$ are updated as follows:

$$\mathbf{P}_{k|k} = \mathbf{P}_{k|k-1} - \mathbf{K}_k \mathbf{P}_{zz,k} \mathbf{K}_k^T \tag{39}$$

$$\hat{\mathbf{x}}_{k|k} = \hat{\mathbf{x}}_{k|k-1} + \mathbf{K}_k (\mathbf{z}_k - \hat{\mathbf{z}}_{k|k-1}). \tag{40}$$

where Kalman gain $\mathbf{K}_k$ can be obtained by

$$\mathbf{K}_k = \mathbf{P}_{xz,k} \mathbf{P}_{zz,k}^{-1}. \tag{41}$$

Note that it is not guaranteed that the mean of the predicted quaternion in (33) will have a unit norm. To prevent such a case, unconstrained 3D vectors utilizing GRP that represent the attitude error have been adopted in this paper [42].

Let $\boldsymbol{\chi}_{i,k}^{\delta \mathbf{p}_k} \in \mathbb{R}^{3\times(2L+1)}$ be the corresponding sigma points for the attitude error vector $\delta \mathbf{p}_k$. Then, $\hat{\mathbf{q}}_{i,k|k}$ can be obtained by

$$\begin{cases} \hat{\mathbf{q}}_{0,k|k} = \hat{\mathbf{q}}_{k|k} & \text{for } i = 0 \\ \hat{\mathbf{q}}_{i,k|k} = \delta \mathbf{q}_{i,k|k} \otimes \hat{\mathbf{q}}_{k|k} & \text{for } i = 1, \cdots, 2L. \end{cases} \tag{42}$$

where $\delta \mathbf{q}_{i,k|k} = \begin{bmatrix} \boldsymbol{\delta \varrho}_{i,k|k}^T, & \delta q_{i,k|k} \end{bmatrix}^T$ can be defined by

$$\delta q_{i,k|k} = \frac{-a \left\| \boldsymbol{\chi}_{i,k}^{\delta \mathbf{p}_k} \right\|^2 + f \sqrt{f^2 + (1-a^2) \left\| \boldsymbol{\chi}_{i,k}^{\delta \mathbf{p}_k} \right\|^2}}{f^2 + \left\| \boldsymbol{\chi}_{i,k}^{\delta \mathbf{p}_k} \right\|^2} \tag{43}$$

$$\boldsymbol{\delta \varrho}_{i,k|k}^T = f^{-1} \left[a + \delta q_{i,k|k} \right] \boldsymbol{\chi}_{i,k}^{\delta \mathbf{p}_k} \tag{44}$$

Then, the predicted quaternion is updated using (23), with

$$\hat{\mathbf{q}}_{i,k+1|k} = \hat{\mathbf{q}}_{k|k} + \frac{1}{2} \hat{\mathbf{q}}_{i,k|k} \otimes \left\{ (\boldsymbol{\omega}_m - \boldsymbol{\chi}_{i,k}^{\omega_\mathbf{b}}) T_s \right\}, \quad i = 0, \cdots, 2L. \tag{45}$$

where $\boldsymbol{\chi}_{i,k}^{\omega_\mathbf{b}} \in \mathbb{R}^{3\times(2L+1)}$ denotes the corresponding sigma points for the gyroscope biases.

The propagated error quaternion is obtained utilizing

$$\delta \mathbf{q}_{i,k+1|k} = \hat{\mathbf{q}}_{i,k+1|k} \otimes \hat{\mathbf{q}}_{0,k+1|k}^{-1}, \quad i = 0, \cdots, 2L. \tag{46}$$

Note that $\delta \mathbf{q}_{0,k+1|k}$ is the identity quaternion. The propagated sigma point for the attitude error can be obtained by

$$\begin{cases} \boldsymbol{\chi}_{0,k+1}^{\delta \mathbf{p}_k} = 0 & \text{for } i = 0 \\ \boldsymbol{\chi}_{i,k+1}^{\delta \mathbf{p}_k} = f \frac{\boldsymbol{\delta \varrho}_{i,k+1|k}}{a + \delta q_{i,k+1|k}} & \text{for } i = 1, \cdots, 2L. \end{cases} \tag{47}$$

with $\begin{bmatrix} \boldsymbol{\delta \varrho}_{i,k+1|k}, & \delta q_{i,k+1|k} \end{bmatrix}^T = \delta \mathbf{q}_{i,k+1|k}$.

Then, the quaternion is updated utilizing

$$\hat{\mathbf{q}}_{k+1|k+1} = \delta \mathbf{q}_{k+1|k+1} \otimes \hat{\mathbf{q}}_{0,k+1|k} \tag{48}$$

where $\delta \mathbf{q}_{k+1|k+1} = \begin{bmatrix} \boldsymbol{\delta \varrho}_{k+1|k+1}, & \delta q_{k+1|k+1} \end{bmatrix}^T$ can be expressed by

$$\delta q_{k+1|k+1} = \frac{-a \left\| \boldsymbol{\chi}_k^{\delta \mathbf{p}_{k+1}} \right\|^2 + f \sqrt{f^2 + (1-a^2) \left\| \boldsymbol{\chi}_k^{\delta \mathbf{p}_k} \right\|^2}}{f^2 + \left\| \boldsymbol{\chi}_k^{\delta \mathbf{p}_{k+1}} \right\|^2} \tag{49}$$

$$\boldsymbol{\delta \varrho}_{k+1|k+1}^T = f^{-1} \left[a + \delta q_{k+1|k+1} \right] \boldsymbol{\chi}_k^{\delta \mathbf{p}_{k+1}} \tag{50}$$

Then, $\delta \mathbf{p}_{k+1}$ is reset to zero for the next time step [42].

TABLE II
Geometric/inertial Specifications for KARI EAV-3

Description	Symbol	EAV-3
Wing span	b	$19.5\,\mathrm{m}$
Wing area	S	$21.84\,\mathrm{m}^2$
Mean aerodynamic chord	$\bar{c}$	$3.4\,\mathrm{m}$
Mass	m	$53\,\mathrm{kg}$

TABLE III
Accelerometer and gyroscope specifications [38]

Accelerometer	Specification		
	a_{mx}	a_{my}	a_{mz}
White noise ($E\left[\mathbf{w}_k\mathbf{w}_k{}^T\right]$)	$6.06\cdot10^{-4}(\mathrm{m/s^2})^2$	$9.62\cdot10^{-4}(\mathrm{m/s^2})^2$	$9.85\cdot10^{-4}(\mathrm{m/s^2})^2$
First-order GM Model (τ_a)	1583 (s)	926 (s)	788 (s)
First-order GM Model ($E\left[\mathbf{n}_k\mathbf{n}_k{}^T\right]$)	$0.0219\,(\mathrm{m/s^2})^2$	$0.0168(\mathrm{m/s^2})^2$	$0.0155(\mathrm{m/s^2})^2$
Gyroscope	**Specification**		
	p	q	r
White noise ($E\left[\mathbf{w}_k\mathbf{w}_k{}^T\right]$)	$1.11\cdot10^{-5}(\mathrm{rad/s})^2$	$2.31\cdot10^{-5}(\mathrm{rad/s})^2$	$1.92\cdot10^{-5}(\mathrm{rad/s})^2$
First-order GM Model (τ_ω)	461 (s)	660 (s)	1347 (s)
First-order GM Model ($E\left[\mathbf{n}_k\mathbf{n}_k{}^T\right]$)	$4.61\cdot10^{-4}(\mathrm{rad/s})^2$	$4.69\cdot10^{-4}(\mathrm{rad/s})^2$	$5.71\cdot10^{-4}(\mathrm{rad/s})^2$

TABLE IV
Aerodynamic coefficient parameters of KARI EAV-3 [5]

Description	Symbol	KARI EAV-3
Rolling moment coefficient with respect to sideslip angle	$C_{l\beta}$	$-0.0547\,\mathrm{rad}^{-1}$
Rolling moment coefficient with respect to rudder deflection angle	$C_{l\delta_R}$	$0.0033\,\mathrm{rad}^{-1}$
Rolling moment coefficient with respect to yaw rate	C_{lr}	$0.3491\,\mathrm{rad}^{-1}$
Rolling moment coefficient with respect to roll rate	C_{lp}	$-0.5533\,\mathrm{rad}^{-1}$
Pitching moment coefficient with respect to zero angle of attack	C_{m0}	$-0.0586\,\mathrm{rad}^{-1}$
Pitching moment coefficient with respect to angle of attack	$C_{m\alpha}$	$-1.325\,\mathrm{rad}^{-1}$
Pitching moment coefficient with respect to elevator deflection angle	$C_{m\delta_E}$	$-1.885\,\mathrm{rad}^{-1}$
Pitching moment coefficient with respect to pitch rate	C_{mq}	$-19.221\,\mathrm{rad}^{-1}$
Yawing moment coefficient with respect to sideslip angle	$C_{n\beta}$	$0.0552\,\mathrm{rad}^{-1}$
Yawing moment coefficient with respect to rudder deflection angle	$C_{n\delta_R}$	$-0.0498\,\mathrm{rad}^{-1}$
Yawing moment coefficient with respect to yaw rate	C_{nr}	$-0.0626\,\mathrm{rad}^{-1}$
Yawing moment coefficient with respect to pitch rate	C_{np}	$-0.1725\,\mathrm{rad}^{-1}$

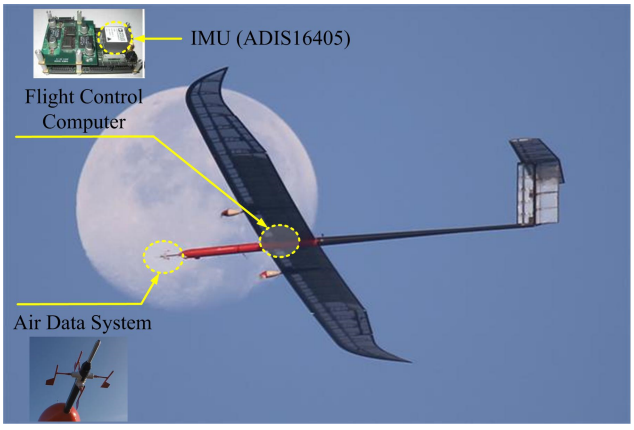

Fig. 2: Images of KARI EAV-3 during the flight test.

V. Experiments

The flight tests were conducted using KARI EAV-3 as shown in Fig. 2. The KARI EAV-3 is a solar-powered HALE UAV that is designed for long-term operation in extreme environments of $-70^{\circ}\mathrm{C}$ in the stratosphere at altitudes above $18\,\mathrm{km}$. The KARI

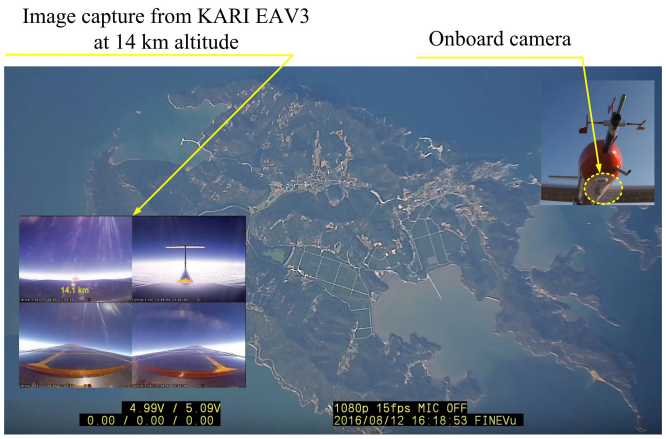

Fig. 3: Image capture from KARI EAV-3 during flight.

TABLE V
KARI EAV-3 inertial parameters [5]

Description	Symbol	KARI EAV-3
Moment of Inertia (x-axis)	I_{xx}	$405.726\,\mathrm{kg}-\mathrm{m}^2$
Moment of Inertia (y-axis)	I_{yy}	$158.301\,\mathrm{kg}-\mathrm{m}^2$
Moment of Inertia (z-axis)	I_{zz}	$558.445\,\mathrm{kg}-\mathrm{m}^2$
Moment of Inertia (x-z axis)	I_{xz}	$12.794\,\mathrm{kg}-\mathrm{m}^2$

TABLE VI
Measurement noise sources of KARI EAV-3

Measurement noise $\mathbf{R}$	
V_m	$1\cdot10^{-3}(\mathrm{m/s})^2$
α_m	$1\cdot10^{-5}(\mathrm{rad})^2$
β_m	$1\cdot10^{-5}(\mathrm{rad})^2$
p_m	$4.69\cdot10^{-4}(\mathrm{rad/s})^2$
q_m	$4.69\cdot10^{-4}(\mathrm{rad/s})^2$
r_m	$5.71\cdot10^{-4}(\mathrm{rad/s})^2$
$\mathbf{v}_g^n$	$1\cdot10^{-3}(\mathrm{m/s})^2$

EAV-3 is equipped with a custom-built autopilot, a GNSS/INS system (UAF-C700, Uconsystem co. ltd), an IMU (ADIS16405, Analog Devices), a barometric pressure sensor (MS5611-01BA03, TE Connectivity), custom-built airspeed sensor, AOA/SSA vanes, and a GNSS receiver (NEO-M8N, Ublox). Table II represents the detailed specifications of KARI EAV-3. The statistical specification of an IMU obtained from Allan variance is given in Table III.

The airframe shape design and static stability derivatives of KARI EAV-3 were designed using the Advanced Aircraft Analysis Software Package (AAA), an aircraft design program, and verified by computational analysis with Fluent ANSYS [5]. The obtained aerodynamic and stability derivatives of KARI EAV-3 through the analysis and wind tunnel testing are summarized in Table IV [5]. The inertial parameters of KARI EAV-3 are provided in Table V. For the UKF implementation, α_u, β_u, and κ_u are set to 0.5, 2, and 0, respectively. T_s was set to 0.1 s, and the measurement noise sources are summarized in Table VI.

VI. Results and Discussion

A. Algorithms descriptions

To demonstrate the effectiveness of the proposed model-aided algorithm, the model-aided navigation algorithm that does not consider 3D wind states [29], denoted as the wind-free algorithm and the proposed algorithm, was implemented for the estimation performance comparison. In contrast to the proposed algorithm, the wind-free algorithm does not consider the effect of the 3D wind, thereby yielding the following relationship [29]:

$$\mathbf{v}_g^n = \mathbf{R}_b^n(\mathbf{q})\mathbf{v}_a^b. \tag{51}$$

Fig. 4: Commercial GNSS/INS system (Model UAFC-700).

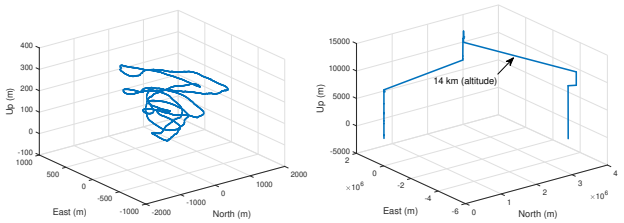

(a) (b)

Fig. 5: Flight trajectories during (a) flight experiment 1 and (b) flight experiment 2.

TABLE VII
The state and measurement definitions for different algorithms

	Algorithms		
	Wind-free [29]	Proposed	Proposed (gyro-free)
States	$\mathbf{x}_k = \begin{bmatrix} V \\ \alpha \\ \beta \\ p \\ q \\ r \\ \delta\mathbf{p} \\ \mathbf{a}_b \\ \boldsymbol{\omega}_b \end{bmatrix}$ – Airspeed – AOA – SSA } Angular rates – Attitude error – Accelerometer bias – Gyroscope bias	$\mathbf{x}_k = \begin{bmatrix} V \\ \alpha \\ \beta \\ p \\ q \\ r \\ \delta\mathbf{p} \\ \mathbf{a}_b \\ \boldsymbol{\omega}_b \\ \mathbf{v}_w^n \end{bmatrix}$ – Airspeed – AOA – SSA } Angular rates – Attitude error – Accelerometer bias – Gyroscope bias – 3D wind	$\mathbf{x}_k = \begin{bmatrix} V \\ \alpha \\ \beta \\ p \\ q \\ r \\ \delta\mathbf{p} \\ \mathbf{a}_b \\ \mathbf{v}_w^n \end{bmatrix}$ – Airspeed – AOA – SSA } Angular rates – Attitude error – Accelerometer bias – 3D wind
	Wind-free [29]	Proposed	Proposed (gyro-free)
Measurement	$\mathbf{z}_k = \begin{bmatrix} V_m \\ \alpha_m \\ \beta_m \\ p_m \\ q_m \\ r_m \\ \mathbf{v}_g^n \end{bmatrix}$ – Airspeed – AOA – SSA } Angular rates – GNSS velocity	$\mathbf{z}_k = \begin{bmatrix} V_m \\ \alpha_m \\ \beta_m \\ p_m \\ q_m \\ r_m \\ \mathbf{v}_g^n \end{bmatrix}$ – Airspeed – AOA – SSA } Angular rates – GNSS velocity	$\mathbf{z}_k = \begin{bmatrix} V_m \\ \alpha_m \\ \beta_m \\ \mathbf{v}_g^n \end{bmatrix}$ – Airspeed – AOA – SSA – GNSS velocity

Additionally, to verify the feasibility of the proposed algorithm in the case where the gyroscope signals are unavailable, the proposed algorithm is tested in the absence of gyroscope measurements, denoted as proposed (gyro-free). Note that we decided to implement the algorithm with the gyroscope signals completely omitted from the filter to rigorously demonstrate the effectiveness of the proposed algorithm in response to gyroscope failures. With the aid of a fault detection scheme, the gyro-free algorithm could be implemented as needed within flight applications. For clarity, the states and measurement definitions of the wind-free, proposed, and proposed (gyro-free) algorithms are summarized in Table VII. Although the fault detection scheme is beyond the scope of this paper, the proposed (gyro-free) algorithm can work with several fault detection algorithms such as the chi-square and sequential probability ratio test (SPRT) fault detection described in our previous study [43].

B. Nonlinear Observability Analysis

Observability is an important consideration when designing state estimation filters. The observability of the system, by definition, is the ability to determine the state $\mathbf{x}_k$ from a finite history of measurements $\mathbf{z}_k$. That is, observability indicates that the measurement is able to provide sufficient information in order to determine the state of the system [44]. If a system is not observable, the states are not able to be uniquely determined using the considered measurements. For time-invariant linear systems, a convenient test such as the rank of the Gramian matrix [45] or Popov-Belevitch-Hautus (PBH) test [46] can be utilized to check whether a system is observable. Observability for nonlinear systems, however, is a bit more complex. One method of determining the observability of a nonlinear system is by computing the rank of the observability matrix based on

TABLE VIII
Observability analysis results

	Algorithms	
	Proposed	Proposed (gyro-free)
State dimension	18	15
Rank	$\text{rank}(\Xi) = 17$	$\text{rank}(\Xi) = 14$

Lie derivatives [44]. For instance, the observability matrix based on Lie derivatives was conducted for applications such as robust pose estimation of quadrotor UAVs using monocular vision [47] and cooperative localization of ground vehicle in [48].

Following the methods presented within [44], [47], [48], the continuous system $f_c(\cdot)$ and observation equations $h(\cdot)$ for an observability analysis can be expressed as follows:

$$\begin{cases} \dot{\mathbf{x}} = f_c(\mathbf{x}, \mathbf{u}) \\ \mathbf{z} = h(\mathbf{x}) \end{cases} \tag{52}$$

where $\mathbf{z} = [z_1, \ldots, z_m]^T \in \mathbb{R}^m$ is the measurement vector with $z_k = h_k(\mathbf{x})\,(k = 1, \ldots, m)$. This system does not consider the process and measurement noise terms from (9) and (10) since it has been shown that these terms should not affect the observability [44]. The zeroth-order Lie derivative of any scholar function is the function itself, thus yielding $L^0 h_k(\mathbf{x}) = h_k(\mathbf{x})$. Then, the first-order Lie derivative of $h_k(\mathbf{x})$ with regard to $f_c(\mathbf{x}, \mathbf{u})$ is given by

$$L_f^1 h_k(\mathbf{x}) = \nabla h_k(\mathbf{x}) \cdot f_c(\mathbf{x}, \mathbf{u}) = \nabla L^0 h_k(\mathbf{x}) \cdot f_c(\mathbf{x}, \mathbf{u}) \tag{53}$$

where "∇" and "$\cdot$" denote the gradient operator and inner product, respectively. Similarly, the second-order Lie derivative $L_f^2 h_k(\mathbf{x})$ with regard to $f_c(\mathbf{x}, \mathbf{u})$ is given by

$$\begin{aligned} L_f^2 h_k(\mathbf{x}) &= L_f^1 \left(L_f^1 h_k(\mathbf{x}) \right) \\ &= \nabla L_f^1 h_k(\mathbf{x}) \cdot f_c(\mathbf{x}, \mathbf{u}) \end{aligned} \tag{54}$$

Then, the observability matrix Ξ based on the Lie derivatives can be defined by [44]

$$\Xi \triangleq \left[\nabla L_f^l h_k(\mathbf{x}) | k = 1, \ldots, m; l = 0, \ldots, n-1 \right] \tag{55}$$

The nonlinear system is locally observable if the observability matrix is full rank [44]. There is currently no systematic method for selecting appropriate Lie derivatives and corresponding rows of Ξ when conducting an observability analysis [49]. Instead, Lie derivatives and corresponding rows of Ξ are typically selected by sequentially considering the gradient which provides information for each of the candidate Lie derivatives. The observability matrix for the proposed model is given as (56)

$$\Xi = \begin{bmatrix} \nabla L^0 h_k(\mathbf{x}) \\ \nabla L_f^1 h_k(\mathbf{x}) \\ \vdots \\ \nabla L_f^{n-1} h_k(\mathbf{x}) \end{bmatrix} \in \mathbb{R}^{n \times m} \tag{56}$$

MATLAB symbolic toolbox was used to perform symbolic rank tests to analyze the observability of the three considered algorithms, with results summarized in Table VIII. Thus, from Table VIII, it is shown that the proposed system and measurement models for the proposed and proposed (gyro-free) algorithms have rank 17 and 14 instead of full rank 18 and 15, respectively. The one unobservable state was identified as the accelerometer bias in y-direction (i.e., a_{by}).

This observation can be explained by the simplified state formulation that does not consider absolute position and velocity states that are commonly implemented within GNSS/INS systems in order to regulate drift caused by integrating IMU signal biases. Additionally, since typically only small accelerations are experienced by aircraft in the y-direction, any bias in this direction would be difficult to distinguish from the actual signal due to a small signal-to-noise ratio. Thus, the one unobservable state is eliminated in the state formulation to prevent the negative effect of the estimation performance due to observability issues. For more details, please see the corresponding MATLAB codes for observability analysis which have been made publicly available at https://www.researchgate.net/profile/Wonkeun_Youn.

TABLE IX
Statistics of attitude estimation performance

RMSE (°)	Flight experiment 1			Flight experiment 2		
	Wind-free [29]	Proposed	Proposed (gyro-free)	Wind-free [29]	Proposed	Proposed (gyro-free)
Roll	0.4129	0.3968	1.1708	0.6057	0.3447	0.8695
Pitch	0.6554	0.5007	0.9949	1.9393	0.4845	0.8204
Yaw	6.3839	5.8107	5.9993	19.1282	19.4469	22.3190

TABLE X
Statistics of angular rate estimation performance

RMSE (rad/s)	Flight experiment 1			Flight experiment 2		
	Wind-free [29]	Proposed	Proposed (gyro-free)	Wind-free [29]	Proposed	Proposed (gyro-free)
p	$1.228 \cdot 10^{-3}$	$1.101 \cdot 10^{-3}$	$13.0599 \cdot 10^{-2}$	$0.2639 \cdot 10^{-3}$	$0.2389 \cdot 10^{-3}$	$11.1005 \cdot 10^{-2}$
q	$1.7615 \cdot 10^{-3}$	$1.2951 \cdot 10^{-3}$	$8.6356 \cdot 10^{-2}$	$4.4386 \cdot 10^{-3}$	$1.2047 \cdot 10^{-3}$	$7.3381 \cdot 10^{-2}$
r	$1.1533 \cdot 10^{-3}$	$1.1432 \cdot 10^{-3}$	$6.8726 \cdot 10^{-2}$	$1.2780 \cdot 10^{-3}$	$1.0299 \cdot 10^{-3}$	$4.5774 \cdot 10^{-2}$

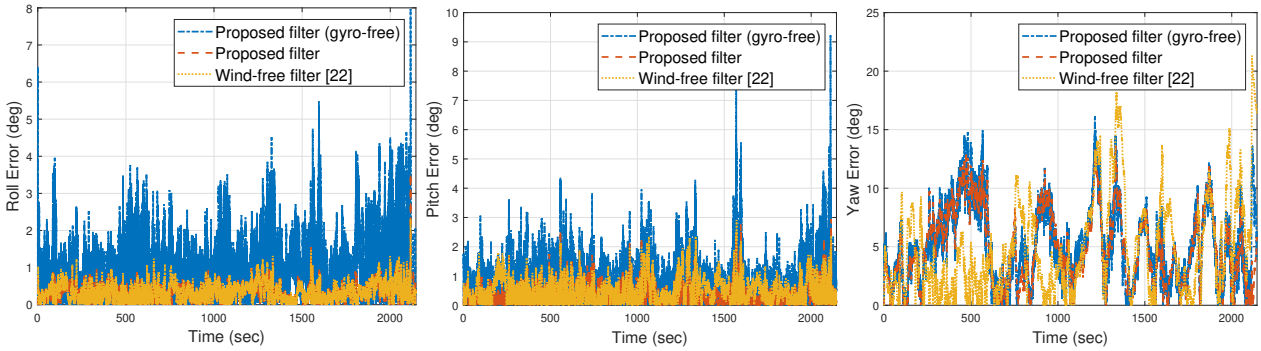

(a) (b) (c)

Fig. 6: Estimation error results of (a) roll, (b) pitch, and (c) yaw during flight experiment 1.

C. Performance evaluation

To obtain the true attitude, the commercial GNSS/INS system (UAF-C700) developed by Uconsystem co. ltd was utilized in this paper, as shown in Fig. 4. The accuracies of the roll/pitch and heading are reported to be 0.6 and 1.0 degrees, respectively. The three above-mentioned algorithms were performed on a laptop computer (Intel i7-6500U CPU) utilizing MATLAB 2016b. The root mean square errors (RMSEs) for the angular rate and attitude were utilized to analyze the estimation performance.

$$\text{RMSE} = \sqrt{\frac{1}{T}\sum_{k=1}^{T}(\mathbf{x}_k - \hat{\mathbf{x}}_k)^2}. \tag{57}$$

Two sets of flight experiments were performed at the aeronautical center of KARI (Goheung, Republic of Korea). Flight experiment 1 was a preliminary test conducted for 35.76 minutes. Flight experiment 2 was performed as an eight-hour flight test (approximately 481 minutes) to further verify the effectiveness of the proposed algorithm, and KARI EAV-3 reached an altitude of 14 km. Fig. 3 shows the image capture from KARI EAV-3 at 14.1 km altitude during flight experiment 2. Fig. 5(a) and (b) depict the navigation trajectory for flight experiments 1 and 2, respectively.

Fig. 6(a), (b), and (c) show the absolute error of the Euler angle during flight experiment 1. As shown, the proposed algorithm results in better estimation performance than the wind-free algorithm. Fig. 7(a), (b), and (c) represent the absolute error of the Euler angle during flight experiment 2. Additionally, the attitude estimation of the proposed algorithm is more accurate than the wind-free algorithm. Note that the performance improvement of the proposed model-aided algorithm during flight experiment 2 is more profound than that of flight experiment 1 because flight experiment 2, which flew at a higher altitude, experienced stronger wind effects than flight experiment 1. Tables IX and X summarize the estimation performances of the attitude and angular rate of the wind-free and proposed filters, respectively. It can thus be concluded that the proposed dynamic model-aided filter, considering the effects of 3D wind states, can more accurately estimate the attitude and angular rate than the wind-free filter. In addition, the attitude and angular rate estimations of the proposed filter (gyro-free) still yield accurate results even though the accuracy is lower than the wind-free and proposed algorithms when utilizing the gyroscope signals. A fairly large yaw estimation error is noted within Table IX, particularly for flight experiment 2. Although the absolute error is large, the relative estimation performance between the gyro-free algorithm is not significantly degraded when compared to the

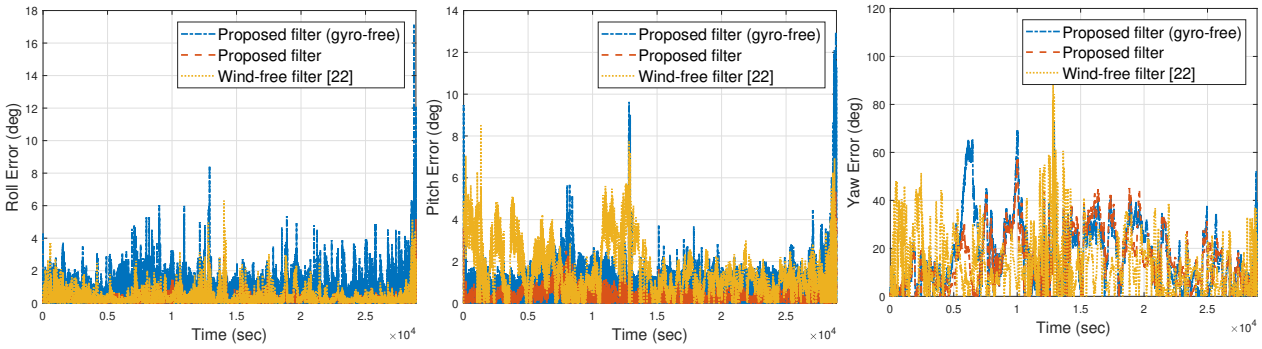

(a) (b) (c)

Fig. 7: Estimation error results of (a) roll, (b) pitch, and (c) yaw during flight experiment 2.

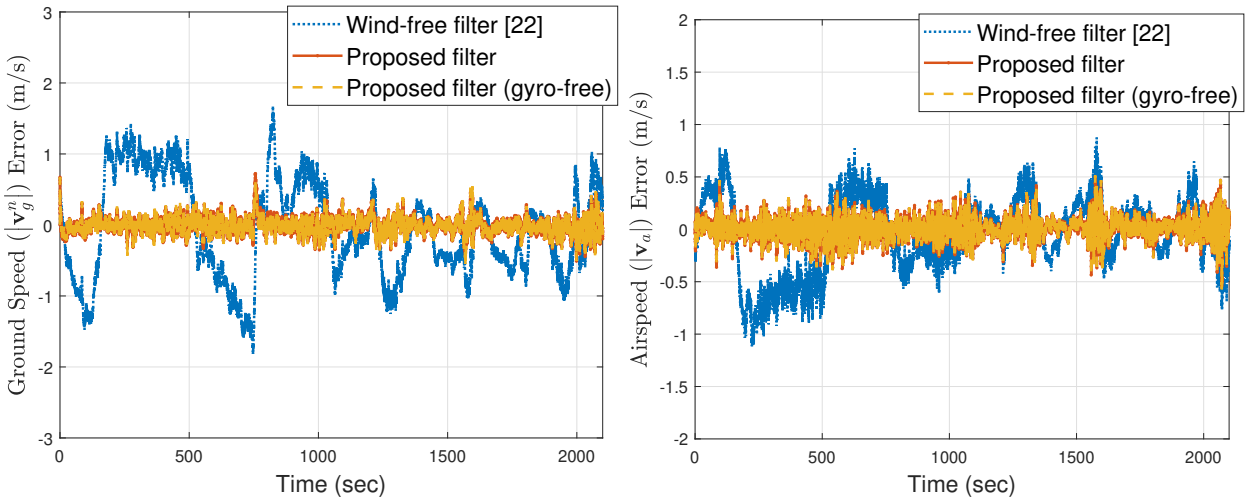

(a) (b)

Fig. 8: Estimation error results of (a) ground speed and (b) airspeed during flight experiment 1.

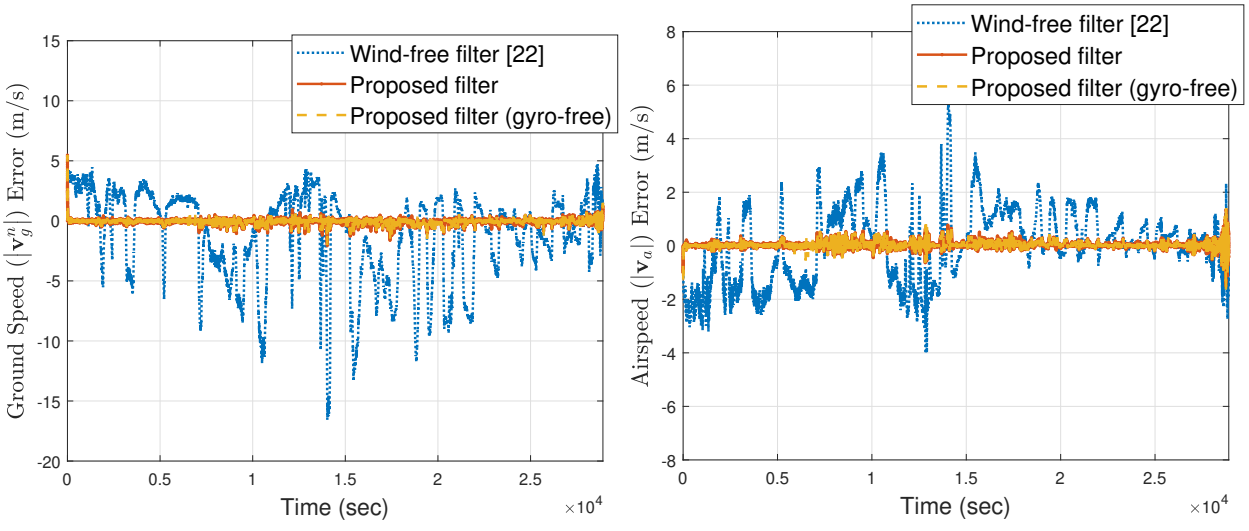

(a) (b)

Fig. 9: Estimation error results of (a) ground speed and (b) airspeed during flight experiment 2.

other algorithms. The consistently higher absolute error for yaw is likely due to misalignment between the estimated data and the reference data, and is not a significant concern within this work.

Fig. 8, 9(a) and (b) show the estimation error of the predicted ground speed with respect to the measured ground speed during

TABLE XI
Statistics of airspeed, AOA, and SSA estimation performance

RMSE	Flight experiment 1			Flight experiment 2		
	Wind-free [29]	Proposed	Proposed (gyro-free)	Wind-free [29]	Proposed	Proposed (gyro-free)
Airspeed (V, unit: m/s)	0.3686	0.0894	0.092	1.3871	0.1076	0.1141
AOA (α, unit: °)	2.1501	2.1515	2.1493	1.8063	1.8118	1.8113
SSA (β, unit: °)	4.8219	4.8217	4.8194	4.0277	4.0291	4.0290

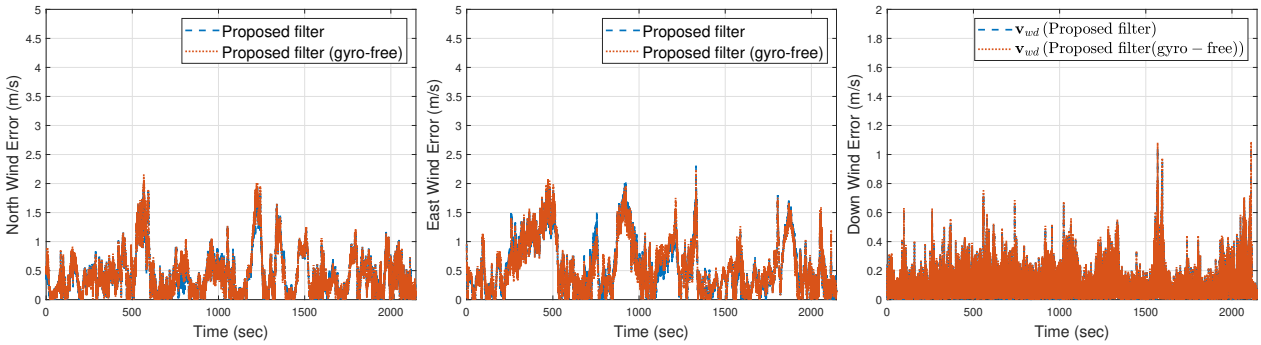

(a) (b) (c)

Fig. 10: Estimation error results of wind states (a) $\mathbf{v}_{wn}$, (b) $\mathbf{v}_{we}$ and (c) $\mathbf{v}_{wd}$ during flight experiment 1.

flight experiment 1 and 2, respectively. Note that the predicted ground speed $\left|\hat{\mathbf{v}}_g^n\right|$ from the proposed and wind-free algorithms are, respectively, computed from (27) and (51) (i.e., $\left|\hat{\mathbf{v}}_g^n\right| = \left|\mathbf{R}_b^n(\hat{\mathbf{q}})\hat{\mathbf{v}}_a^b + \hat{\mathbf{v}}_w^n\right|$ for the proposed algorithm, $\left|\hat{\mathbf{v}}_g^n\right| = \left|\mathbf{R}_b^n(\hat{\mathbf{q}})\hat{\mathbf{v}}_a^b\right|$ for wind-free algorithm). The ground speed and airspeed from the proposed algorithm closely follow the measured ground speed and airspeed from the GNSS receiver and Pitot tube; however, those from the wind-free filter significantly deviate from the measured speeds.

Figs. 10, 11(a) and (b) depict the absolute error of the estimated 3D wind states with respect to the reference 3D wind states during flight experiments 1 and 2, respectively. Additionally, note that reference 3D wind speeds are obtained from the commercial GNSS/INS system (UAF-C700) with 1.4 m/s ($\mathbf{v}_{wn}$/$\mathbf{v}_{we}$) and 0.7 m/s accuracy ($\mathbf{v}_{wd}$) [39]. In several previous studies [11], [12], a ground weather station with approximated wind profiles was utilized to obtain the reference wind speed. However, the altitude of the flight experiment was exceedingly high (e.g., 14 km); thus, the aforementioned approaches are not adequate. As shown in Figs. 10 and 11, the 3D wind estimation of the proposed algorithm closely matches the reference 3D wind from the commercial GNSS/INS system. As explained above, the magnitude of the estimated 3D wind states ($\mathbf{v}_{wn}$, $\mathbf{v}_{we}$, and $\mathbf{v}_{wd}$) by the proposed algorithm during flight experiment 2 are greater than those during flight experiment 1, demonstrating that the wind effect should be considered in the design of the navigation filter when designing a HALE UAV that climbs to high altitudes. In addition, the ground and airspeed of the proposed algorithm (gyro-free) closely match the reference values, indicating that the proposed algorithm (gyro-free) can accurately estimate the 3D wind states without gyroscope signals. In addition, Fig. 12, 13(a) and (b) show the estimation error of airspeed, AOA, and SSA with respect to the measured airspeed, AOA, and SSA during flight experiment 1 and 2, respectively. Table XI summarizes the estimation performances of airspeed, AOA, and SSA of the wind-free and proposed filters, respectively. As shown, the estimation error of AOA and SSA for three filters during the flight experiment 1 and 2 are less than 3.5° and their estimation performances are almost comparable. This result may be due to the direct measurement of AOA and SSA from equipped AOA/SSA vanes for three filters. However, the estimation accuracy of the airspeed of the proposed filters are significantly better than that of the wind-free filter.

This result has significant implications in that the proposed algorithm is designed with the minimum number of states (without the position states) to ensure the safety of the flight while lowering the complexity for ease of implementation. In other words, if the accurate estimation of attitude, 3D wind, airspeed, AOA, and SSA is available, the HALE UAV can be safely controlled under the manual control of the pilot. The study also proves that the proposed algorithm, which newly considers 3D wind states in the dynamic model framework, significantly outperformed the wind-free algorithm in terms of estimation accuracy. In addition, this study first demonstrated the feasibility of the proposed algorithm (gyro-free) based on the dynamic model as the analytical redundancy in the case of gyroscope fault, proving that the drift of the attitude estimation is effectively mitigated in the total absence of gyroscope signals.

VII. Conclusion

This paper presents a novel dynamic model-based estimator for the attitude, 3D wind, AOA, and SSA of a HALE UAV. Specifically, the effect of 3D wind states using the dynamic model is newly introduced in the proposed algorithm, in which

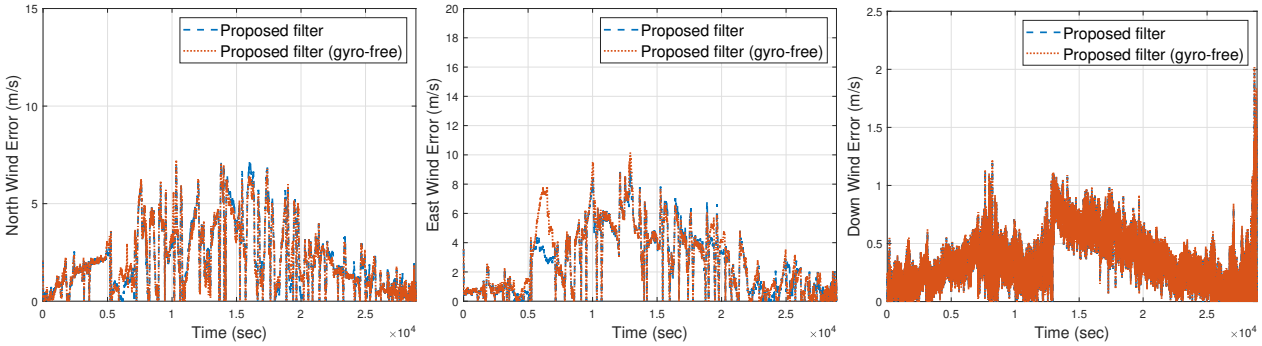

(a) (b) (c)

Fig. 11: Estimation error results of wind states (a) $\mathbf{v}_{wn}$, (b) $\mathbf{v}_{we}$ and (c) $\mathbf{v}_{wd}$ during flight experiment 2.

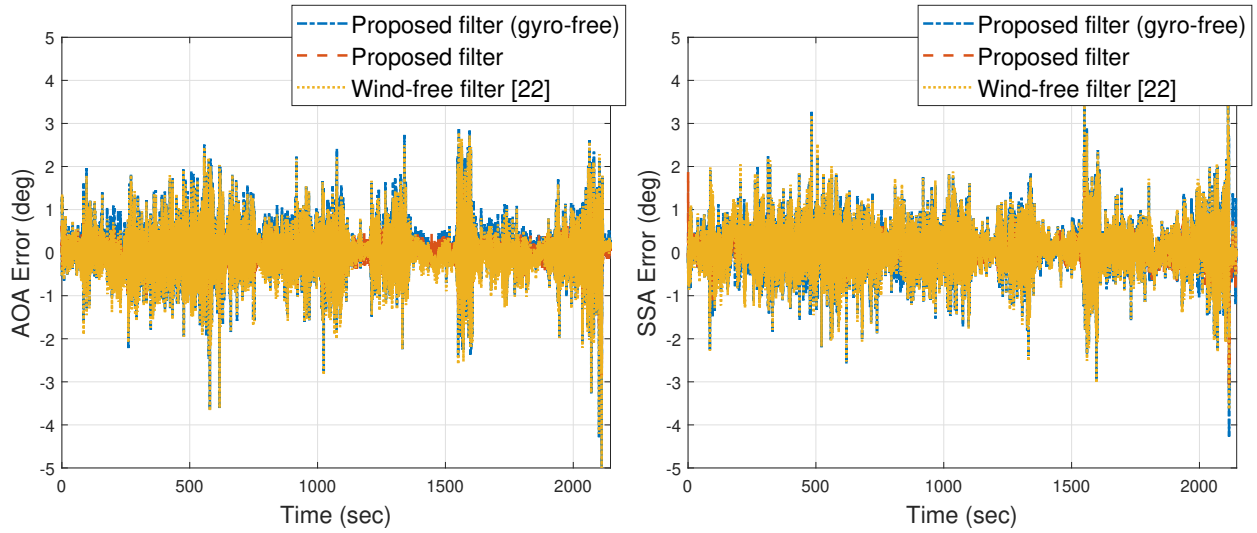

(a) (b)

Fig. 12: Estimation error results of (a) AOA and (b) SSA during flight experiment 1.

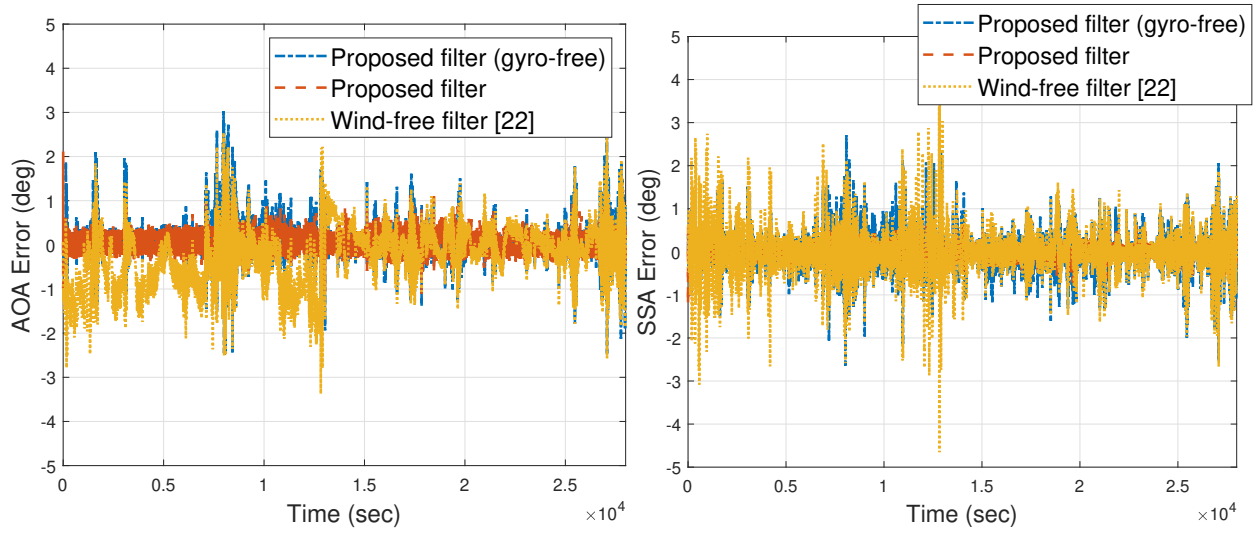

(a) (b)

Fig. 13: Estimation error results of (a) AOA and (b) SSA during flight experiment 2.

the 3D wind states are modelled as RW processes. Moreover, new filter formulations that utilize the accelerometer, elevator,

aileron, and rudder deflection as the control input for the prediction of the gyroscope, Pitot probe, AOA/SSA vanes, and GNSS information for the measurement update are proposed. In particular, the rolling, pitching, and yawing moment as well as the inertial aerodynamic coefficient parameters obtained from the design of a HALE UAV are utilized to predict the angular rate in the proposed algorithm, thus enabling accurate state estimation in the absence of gyroscope signals.

The experimental results demonstrated that the proposed model-aided algorithm results in significant improvements in the attitude and angular rate estimation compared with a model-aided navigation algorithm that does not consider wind. Additionally, the proposed algorithm is capable of producing accurate 3D wind estimates that can be used for navigation within a flow field and allow for accurate ground and airspeed estimates. More importantly, this study successfully demonstrated the feasibility of the proposed algorithm for analytical redundancy for gyroscopes when the gyroscope signals are completely unavailable.

REFERENCES

[1] W. Youn, M. Rhudy, A. Cho, and H. Myung, "Fuzzy Adaptive Attitude Estimation for a Fixed-Wing UAV with a Virtual SSA Sensor During a GPS Outage," *IEEE Sens. J.*, Early Access, Nov. 2019. https://doi.org/10.1109/JSEN.2019.2947489

[2] P. Lu, L. Van Eykeren, E. Van Kampen, C. De Visser, and Q. Chu, "Adaptive three-step Kalman filter for air data sensor fault detection and diagnosis," *J. Guid. Control Dyn.*, pp. 590–604, Aug. 2015.

[3] P. Lu, L. Van Eykeren, E.-J. van Kampen, C. de Visser, and Q. Chu, "Double-model adaptive fault detection and diagnosis applied to real flight data," *Control Eng. Pract.*, vol. 36, pp. 39–57, Mar. 2015.

[4] J.-S. Lee and K.-H. Yu, "Optimal path planning of solar-powered UAV using gravitational potential energy," *IEEE Trans. Aerosp. Electron. Syst.*, vol. 53, no. 3, pp. 1442–1451, Jun. 2017.

[5] S.-J. Hwang, S.-G. Kim, C.-W. Kim, and Y.-G. Lee, "Aerodynamic design of the solar-powered high altitude long endurance (hale) unmanned aerial vehicle (UAV)," *Int. J. Aeronaut. Space Sci.*, vol. 17, no. 1, pp. 132–138, Mar. 2016.

[6] B. Raghavan and M. J. Patil, "Flight control for flexible, high-aspect-ratio flying wings," *J. Guid. Control Dyn.*, vol. 33, no. 1, pp. 64–74, Jan. 2010.

[7] T. A. Johansen, A. Cristofaro, K. Sørensen, J. M. Hansen, and T. I. Fossen, "On estimation of wind velocity, angle-of-attack and sideslip angle of small UAVs using standard sensors," in *2015 International Conference on Unmanned Aircraft Systems (ICUAS)*, pp. 510–519. IEEE, 2015.

[8] M. B. Rhudy, T. Larrabee, H. Chao, Y. Gu, and M. Napolitano, "UAV attitude, heading, and wind estimation using GPS/INS and an air data system," in *AIAA Guidance, Navigation, and Control (GNC) Conference*, p. 5201, 2013.

[9] J. H. Lee, H. E. Sevil, A. Dogan, and D. Hullender, "Estimation of maneuvering aircraft states and time-varying wind with turbulence," *Aerosp. Sci. Technol.*, vol. 31, no. 1, pp. 87–98, Dec. 2013.

[10] J. N. Gross, Y. Gu, M. B. Rhudy, S. Gururajan, and M. R. Napolitano, "Flight-test evaluation of sensor fusion algorithms for attitude estimation," *IEEE Trans. Aerosp. Electron. Syst.*, vol. 48, no. 3, pp. 2128–2139, Jul. 2012.

[11] M. B. Rhudy, M. L. Fravolini, M. Porcacchia, and M. R. Napolitano, "Comparison of wind speed models within a pitot-free airspeed estimation algorithm using light aviation data," *Aerosp. Sci. Technol.*, vol. 86, pp. 21–29, Mar. 2019.

[12] M. B. Rhudy, Y. Gu, J. N. Gross, and H. Chao, "Onboard wind velocity estimation comparison for unmanned aircraft systems," *IEEE Trans. Aerosp. Electron. Syst.*, vol. 53, no. 1, pp. 55–66, Feb. 2017.

[13] M. Khaghani and J. Skaloud, "Assessment of VDM-based autonomous navigation of a UAV under operational conditions," *Robot Auton. Syst.*, vol. 106, pp. 152–164, Aug. 2018.

[14] M. Khaghani and J. Skaloud, "Autonomous vehicle dynamic model-based navigation for small UAVs," *Navigation: Journal of The Institute of Navigation*, vol. 63, no. 3, pp. 345–358, Sept. 2016.

[15] H. Mwenegoha, T. Moore, J. Pinchin, and M. Jabbal, "Model-based autonomous navigation with moment of inertia estimation for unmanned aerial vehicles," *Sensors*, vol. 19, no. 11, p. 2467, May 2019.

[16] P. Lyu, J. Lai, J. Liu, H. H. Liu, and Q. Zhang, "A thrust model aided fault diagnosis method for the altitude estimation of a quadrotor," *IEEE Trans. Aerosp. Electron. Syst.*, vol. 54, no. 2, pp. 1008–1019, Nov. 2017.

[17] P. Lyu, J. Lai, H. H. Liu, J. Liu, and W. Chen, "A model-aided optical flow/inertial sensor fusion method for a quadrotor," *J. Navig.*, vol. 70, no. 2, pp. 325–341, Mar. 2017.

[18] D. Abeywardena, S. Kodagoda, G. Dissanayake, and R. Munasinghe, "Improved state estimation in quadrotor mavs: A novel drift-free velocity estimator," *IEEE Robot. Autom. Mag.*, vol. 20, no. 4, pp. 32–39, 2013. https://doi.org/10.1109/MRA.2012.2225472.

[19] D. Abeywardena and G. Dissanayake, "Tightly-coupled model aided visual-inertial fusion for quadrotor micro air vehicles," in *Field and Service Robotics*, pp. 153–166. Switzerland: Springer, 2015.

[20] R. Wang, D. Zou, C. Xu, L. Pei, P. Liu, and W. Yu, "An aerodynamic model-aided state estimator for multi-rotor UAVs," in *2017 IEEE/RSJ International Conference on Intelligent Robots and Systems (IROS)*, pp. 2164–2170. IEEE, 2017.

[21] J. Vasconcelos, C. Silvestre, P. Oliveira, and B. Guerreiro, "Embedded UAV model and laser aiding techniques for inertial navigation systems," *Control Eng. Pract.*, vol. 18, no. 3, pp. 262–278, Mar. 2010.

[22] P. Tian, H. Chao, H. P. Flanagan, S. G. Hagerott, and Y. Gu, "Design and evaluation of UAV flow angle estimation filters," *IEEE Trans. Aerosp. Electron. Syst.*, vol. 55, no. 1, pp. 371–383, Jul. 2018.

[23] P. Tian and H. Chao, "Model aided estimation of angle of attack, sideslip angle, and 3D wind without flow angle measurements," in *2018 AIAA Guidance, Navigation, and Control Conference*, p. 1844, 2018.

[24] M. Koifman and I. Bar-Itzhack, "Inertial navigation system aided by aircraft dynamics," *IEEE Trans. Control Syst. Technol.*, vol. 7, no. 4, pp. 487–493, Jul. 1999.

[25] H. Nobahari and H. Mohammadkarimi, "Application of model aided inertial navigation for precise altimetry of unmanned aerial vehicles in ground proximity," *Aerosp. Sci. Technol.*, vol. 69, pp. 650–658, Oct. 2017.

[26] F. A. P. Lie and D. Gebre-Egziabher, "Synthetic air data system," *J. Aircraft*, vol. 50, no. 4, pp. 1234–1249, Jul. 2013.

[27] P. Lyu, S. Liu, J. Lai, and J. Liu, "An analytical fault diagnosis method for yaw estimation of quadrotors," *Control Eng. Pract.*, vol. 86, pp. 118–128, May 2019.

[28] O.-J. Kim, S. Yu, H. No, C. Kee, M. Choi, H. Seok, D. Yoon, B. Park, and C. Jee, "Navigation augmentation in urban area by hale UAV with onboard pseudolite during multi-purpose missions," *Int. J. Aeronaut. Space Sci.*, vol. 18, no. 3, pp. 545–554, Sept. 2017.

[29] M. Rhudy, "A dynamic model-aided sensor fusion approach to aircraft attitude estimation," in *2017 IEEE 60th International Midwest Symposium on Circuits and Systems (MWSCAS)*, pp. 1406–1409. IEEE, 2017.

[30] G. Araguás, C. Paz, D. Gaydou, and G. P. Paina, "Quaternion-based orientation estimation fusing a camera and inertial sensors for a hovering UAV," *J. Intell. Robot. Syst.*, vol. 77, no. 1, pp. 37–53, 2015.

[31] Y. S. Suh, "Orientation estimation using a quaternion-based indirect Kalman filter with adaptive estimation of external acceleration," *IEEE Instrum. Meas. Mag.*, vol. 59, no. 12, pp.3296–3305, Dec. 2010.

[32] H. No, A. Cho, and C. Kee, "Attitude estimation method for small UAV under accelerative environment," *GPS Solut.*, vol. 19, no. 3, pp. 343–355, Jul. 2015.

[33] W. Li and J. Wang, "Effective adaptive Kalman filter for MEMS-IMU/Magnetometers integrated attitude and heading reference systems," *J. Navig.*, vol. 66, no. 1, pp. 99–113, Jan. 2013.
[34] W. Youn and H. Myung, "Robust interacting multiple model with modeling uncertainties for maneuvering target tracking," *IEEE Access*, vol. 7, pp. 65 427–65 443, May 2019.
[35] V. Klein and E. A. Morelli, *Aircraft System Identification: Theory and Practice*. Virginia: American Institute of Aeronautics and Astronautics Reston, 2006.
[36] R. C. Nelson *et al.*, *Flight Stability and Automatic Control*, vol. 2. New York: WCB/McGraw Hill, 1998.
[37] R. Mahony, M. Euston, J. Kim, P. Coote, and T. Hamel, "A non-linear observer for attitude estimation of a fixed-wing unmanned aerial vehicle without GPS measurements," *T. I. Meas. Control*, vol. 33, no. 6, pp. 699–717, 2011.
[38] J. Gross, Y. Gu, M. Rhudy, F. Barchesky, and M. Napolitano, "On-line modeling and calibration of low-cost navigation sensors," in *AIAA Modeling and Simulation Technologies Conference*, p. 6332, 2011.
[39] A. Cho, J. Kim, S. Lee, and C. Kee, "Wind estimation and airspeed calibration using a UAV with a single-antenna GPS receiver and pitot tube," *IEEE Trans. Aerosp. Electron. Syst.*, vol. 47, no. 1, pp. 109–117, Jan. 2011.
[40] M. Rhudy and Y. Gu, "Understanding nonlinear Kalman filters part 1: Selection of EKF or UKF," *Interactive Robotics Letters*, vol. 1, no. 1, pp. 1–9, 2013.
[41] M. Rhudy and Y. Gu, "Understanding nonlinear Kalman filters, part II: an implementation guide," *Interactive Robotics Letters*, vol. 1, no. 1, pp. 1–18, 2013.
[42] J. L. Crassidis and F. L. Markley, "Unscented filtering for spacecraft attitude estimation," *J. Guid. Control Dyn.*, vol. 26, no. 4, pp. 536–542, May 2003.
[43] W. Youn and S. A. Gadsden, "Combined quaternion-based error state Kalman filtering and smooth variable structure filtering for robust attitude estimation," *IEEE Access*, vol. 7, pp. 148989–149004, 2019.
[44] R. Hermann and A. Krener, "Nonlinear controlability and observability," *IEEE Trans. Autom. Control*, vol. AC-22, no. 5, pp. 728–740, Oct. 1977.
[45] P. S. Maybeck, "Stochastic Models, Estimation and Control," vol. 1. New York: *Academic Press*, 1979.
[46] W. J. Rugh, "Linear System Theory," 2nd ed. Upper Saddle River, NJ: *Prentice-Hall*, 1996.
[47] Q. Fu, Q. Quan, K. Y. Cai, "Robust Pose Estimation for Multirotor UAVs Using Off-Board Monocular Vision," *IEEE Trans. Ind. Electron.*, Vol. 64, No. 10, pp. 7942–7951, Oct. 2017.
[48] A. Martinelli and R. Siegwart, "Observability analysis for mobile robot localization," in *Proc. IEEE/RSJ Int. Conf. Intell. Robots Syst.*, Edmonton, Canada, Aug. 2–6, pp. 1471–1476, 2005.
[49] F. M. Mirzaei and S. I. Roumeliotis, "A Kalman filter-based algorithm for IMU-camera calibration: Observability analysis and performance evaluation," *IEEE Trans. Robot.*, vol. 24, no. 5, pp. 1143–1156, 2008.

Wonkeun Youn received his B.S. degree from Handong Global University, Pohang, South Korea, in 2008 and his M.S. degree from the Korea Advanced Institute of Science and Technology (KAIST), Daejeon, South Korea, in 2010.

He has been a Senior Researcher with the UAV System Division, Korea Aerospace Research Institute (KARI), since 2011 and is currently pursuing his Ph.D. degree at the Department of Robotics Program at KAIST. His current research interests include multi-sensor fusion, Bayesian estimation theory, multi-modal target tracking, and GNSS/INS-based UAV navigation.

Hyoungsik Choi received his Ph.D. degree in aerospace engineering from the Korea Advanced Institute of Science and Technology (KAIST), Daejeon, South Korea, in 2011. He has been a Principal Researcher with the UAV System Division, Korea Aerospace Research Institute (KARI), since 2002. His research interests include flight simulation and control. He has been involved in projects developing UAVs, especially in the design and implementation of software for flight dynamics and control.

Am Cho received his received B.S., M.S., and Ph.D. degrees from Seoul National University (SNU) in 2010, Seoul, South Korea. He was a leader of the UAV team in the GNSS Laboratory. He has been a Senior Researcher with the UAV System Division, Korea Aerospace Research Institute (KARI) since 2010. His research interests include GNSS/INS integration and automatic flight control systems for UAVs.

Sungyug Kim received B.S. degrees in naval architecture and ocean engineering from Inha University in 1987, Incheon, South Korea. He served as a navy Lieutenant from 1987 to 1994. He was a Senior Researcher with the Korea Aerospace Industries, Ltd., Sacheon, from 1994 to 2000. He has been a Principal Researcher with the UAV System Division, Korea Aerospace Research Institute (KARI) since 2001. His research interests include system integration and hardware design. He has been involved in projects developing UAVs, especially in the design and implementation of hardware for flight dynamics and control.

Matthew B. Rhudy received his B.S. degree in mechanical engineering from Pennsylvania State University, State College, PA, USA; his M.S. degree in mechanical engineering from the University of Pittsburgh, Pittsburgh, PA, USA; and his Ph.D. degree in aerospace engineering from West Virginia University, Morgantown, WV, USA, in 2008, 2009, and 2013, respectively. From 2013 to 2015, he worked as a Visiting Assistant Professor at the Department of Mechanical Engineering, Lafayette College, Easton, PA, USA. Since 2015, he has been an Assistant Professor in the Division of Engineering, Pennsylvania State University, Reading, PA, USA.